Received: 6 January 2017 | Revised: 17 March 2017 | Accepted: 24 March 2017

DOI: 10.1002/fld.4381

RESEARCH ARTICLE

WILEY

Improving the robustness of the control volume finite element method with application to multiphase porous media flow

Pablo Salinas[1,2] | Dimitrios Pavlidis[1,2] | Zhihua Xie[1,2,3] | Carl Jacquemyn[1,2] | Yulia Melnikova[1] | Matthew D Jackson[1] | Christopher C Pain[1]

[1]Novel Reservoir Modelling and Simulation Group, Department of Earth Science and EngineeringImperial College London, London, UK

[2]Applied Modelling and Computation Group, Department of Earth Science and Engineering, Imperial College London, London, UK

[3]Now at School of Engineering, Cardiff University, Cardiff, CF24 3AA, UK

Correspondence
Pablo Salinas, Novel Reservoir Modelling and Simulation Group, Department of Earth Science and Engineering, Imperial College London, London, UK.
Email: pablo.salinas@imperial.ac.uk

Funding information
ExxonMobil; EPSRC "Reactor Core-Structure Relocation Modelling for Severe Nuclear Accident"; Horizon 2020 "In-Vessel Melt Retention"; EPSRC ("Multi-Scale Exploration of Multiphase Physics in Flows"—MEMPHIS); TOTAL

Summary

Control volume finite element methods (CVFEMs) have been proposed to simulate flow in heterogeneous porous media because they are better able to capture complex geometries using unstructured meshes. However, producing good quality meshes in such models is nontrivial and may sometimes be impossible, especially when all or parts of the domains have very large aspect ratio. A novel CVFEM is proposed here that uses a control volume representation for pressure and yields significant improvements in the quality of the pressure matrix. The method is initially evaluated and then applied to a series of test cases using unstructured (triangular/tetrahedral) meshes, and numerical results are in good agreement with semianalytically obtained solutions. The convergence of the pressure matrix is then studied using complex, heterogeneous example problems. The results demonstrate that the new formulation yields a pressure matrix than can be solved efficiently even on highly distorted, tetrahedral meshes in models of heterogeneous porous media with large permeability contrasts. The new approach allows effective application of CVFEM in such models.

KEYWORDS

CVFEM mixed formulation, discontinuous galerkin, darcy flow, multiphase flow, porous media, unstructured mesh

1 | INTRODUCTION

The classical approach for simulating multiphase flow in porous media discretises space using fixed grids and solves the governing equations using finite-volume methods and the 2-point flux approximation.[1,2] Although widely used, complex geometries are often poorly represented in this approach because of the limitations of the 2-point flux approximation. Alternative methods use unstructured meshes to discretise space and control volume finite element methods (CVFEMs) or variants thereof to solve the governing equations (see the references herein[3-14]). An unstructured mesh better captures the often complex, multiscale, and time-dependent solution fields such as pressure, saturation, or composition, especially when used in conjunction with dynamic adaptive mesh optimisation.[11,13,14] In most CVFEM schemes, pressure and velocity are discretised finite element (FE)–wise, whereas saturation and composition are discretised control volume (CV)–wise to enforce mass conservation. However, it is well known, although rarely reported in the literature, that solving the pressure equation in such schemes can be very challenging if there are elements with large angles. The pressure solution may fail to converge, or the results may be physically

This is an open access article under the terms of the Creative Commons Attribution License, which permits use, distribution and reproduction in any medium, provided the original work is properly cited.
Copyright © 2017 The Authors International Journal for Numerical Methods in Fluids Published by John Wiley & Sons Ltd

unrealistic.[15-17] A modified CVFEM was proposed by Larreteguy[18] to deal with obtuse elements, but author states that the method should only be used in local regions of the mesh; it should not be used as a global fix for a poor mesh. Since mesh quality is of such importance, a great deal of effort has been devoted to creating good quality meshes (eg, the previous studies [19-24]). However, unless an extremely fine mesh resolution is used, large-angle elements may be inevitable when discretising the very high aspect ratio domains frequently found in geological models (eg, the previous studies[25-28]). Large-angle elements may also be created at displacement fronts when using dynamic adaptive mesh optimisation.[11,13]

Here, a variation of the classical CVFEM is presented, termed the double control volume finite element method (DCVFEM). In this new method, pressure is discretised CV-wise rather than FE-wise. All other variables are discretised following the classical CVFEM. The approach conserves mass and, in the implementation reported here, time is discretised using an adaptive implicit method that provides efficient convergence using highly anisotropic meshes without reducing the time-step size.[29-31] However, it is likely that the new DCVFEM could be implemented with other time-stepping approaches.

The new method is first tested to prove that it can reproduce multiphase flow in a number of simple test cases. Its robustness is then demonstrated using example models containing complex geometries with very large aspect ratio domains and large permeability contrasts, discretised using highly distorted triangular and tetrahedral meshes. The example models represent various complex geological reservoirs and were constructed using a surface-based approach in which heterogeneous domains are represented as volumes bounded by surfaces.[11,32-34] However, the new formulation is not restricted to geological problems. It is suitable for any multiphase porous media flow applications in which heterogeneities, or approaches such as dynamic mesh optimisation, give rise to highly distorted meshes.

The presented results demonstrate that the new DCVFEM creates a good quality pressure matrix that can be solved using widely available solvers even when the mesh contains a significant proportion of elements with very large angles. The new method is novel and significant because it provides a solution to a commonly encountered problem in the use of CVFEM with unstructured meshes to model the large group of problems that include multiphase flow in highly heterogeneous domains.

2 | A DOUBLE CONTROL VOLUME FINITE ELEMENT METHOD

This paper builds on the formulation presented in Gomes et al [35] and focuses on the element pair $P_nDGP_{n+1}(FE)$, in which the velocity is discontinuous across elements and is represented with 1° less than the continuously represented pressure. However, in the classical CVFEM, pressure is represented element-wise and varies continuously across an element (Figure 1A), whereas in this paper, the pressure is represented using CVs and is piecewise constant within a CV (Figure 1B). The notation used for the new method reported here is therefore $P_nDGP_{n+1}(CV)$. As this is the sole difference between the classical CVFEM of Gomes et al [35] and the new DCVFEM reported here, only a summary of the equations and classical formulation will be presented prior to explaining the new DCVFEM with CV pressure representation. We report here how the CV-based pressure system is formulated; other details of the method can be found in Gomes et al.[35]

Darcy's law for multiphase flow can be written as

$$\mathbf{v}_\alpha = \underline{\underline{\sigma}}_\alpha \mathbf{u}_\alpha = -\nabla p_\alpha + \mathbf{s}_{u\alpha}, \tag{1}$$

where $\mathbf{v}_\alpha$ is the force density, $\mathbf{u}_\alpha$ is the phase saturation-weighted Darcy velocity of phase α. p_α is the pressure and $\mathbf{s}_{u_\alpha}$ is a source term, which may include gravity and/or capillary pressure. σ_α is defined as

$$\underline{\underline{\sigma}}_\alpha = \mu_\alpha S_\alpha \left(\mathcal{K}_{r_\alpha}\mathbf{K}\right)^{-1}, \tag{2}$$

where $\mathbf{K}$ is the permeability tensor, $\mathcal{K}_{r_\alpha}$, μ_α, and S_α are the relative permeability, viscosity, and saturation of phase α, respectively.

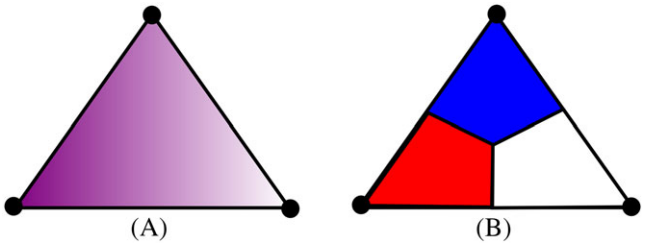

FIGURE 1 Comparison of the pressure representation for a P_1 element with the nodes in the corners of the element, using A, the classical control volume finite element method and B, the novel double control volume finite element method. In panel A, the pressure is defined as a continuous field across the element, whereas in panel B, the pressure is piecewise constant per control volume [Colour figure can be viewed at wileyonlinelibrary.com]

In classical CVFEM, Equation 1 is discretised using an FE-based representation for velocity and pressure. Here, only the velocity is discretised using FE; the pressure is discretised using CV shape functions:

$$\mathbf{v}_\alpha(\boldsymbol{r},t)=\sum_{j=1}^{\mathcal{N}_u} Q_j(\boldsymbol{r})\mathbf{v}_{\alpha,j}(t) \quad \text{and} \quad p(\boldsymbol{r},t)=\sum_{j=1}^{\mathcal{N}_p} P_j(\boldsymbol{r})p_j(t), \tag{3}$$

where Q_j and P_j are FE Lagrangian basis functions and CV Lagrangian basis functions, respectively. $\mathcal{N}_u$ and $\mathcal{N}_p$ are the number of degrees of freedom for the velocity and pressure, respectively. Each component of the weak form of the force balance Equation 1 is tested with the FE Lagrangian basis function to obtain:

$$\sum_E \int_{\Omega_E} Q_i\left(\mathbf{v}_\alpha-\mathbf{s}_{u_\alpha}\right)dV+\sum_j \oint_{\Gamma_{CV_j}-\Gamma_E} Q_i\mathbf{n}P_j p_{CV\,j}d\Gamma+\oint_{\Gamma_\Omega} Q_i\mathbf{n}p_{\mathrm{bc}}d\Gamma=\boldsymbol{0}, \tag{4}$$

where $\boldsymbol{n}$ is the outward-pointing normal vector, Ω_E and Γ_E are the volume and boundary of element E, respectively, and Γ_Ω is the boundary of the computational domain. The last term in Equation 4 is used to weakly enforce the pressure boundary condition, p_{bc}, on the domain boundary.

In matrix form, Equation 4 is

$$\mathbf{M}\underline{\mathbf{v}}=-\mathbf{C}\underline{\mathbf{p}}+\underline{\mathbf{s}}_u, \tag{5}$$

where $\mathbf{v}$ and $\mathbf{p}$ are the solution vectors of velocity and pressure, respectively, defined as

$$\underline{\mathbf{v}}=\left(\left(v_x,v_y,v_z\right)_{1,1},\left(v_x,v_y,v_z\right)_{2,1},\ \dots\ ,\left(v_x,v_y,v_z\right)_{\mathcal{N}_\alpha\mathcal{N}_u}\right)^T \text{ and}$$
$$\underline{\mathbf{p}}=\left(p_1,p_2,p_3,\ \dots\ ,p_{\mathcal{N}_p}\right)^T.$$

$\mathcal{N}_\alpha$ denotes the number of phases; v_x, v_y, and v_z are the components of the velocity associated with each Cartesian dimension (x, y, and z). The mass matrix $\mathbf{M}$, gradient matrix $\mathbf{C}$, and source vector $\mathbf{s}_u$ are defined as

$$\left[\mathbf{M}^{(i,j)}\right]_{k,l}=\int_\Omega Q_k\left[\underline{\underline{\sigma}}_\alpha\right]_{i,j}Q_l dV,$$
$$\left[\boldsymbol{C}^{(i,i)}\right]_{k,l}=\int_\Omega Q_k\frac{\partial P_l}{\partial r_i}dV-\oint_{\Gamma_E}\frac{1}{2}Q_k n_i^{(E,l)}P_l d\Gamma-\oint_{\Gamma_\Omega}Q_k n_i P_l d\Gamma,$$
$$\left[\boldsymbol{s}_u^{(i,i)}\right]_k=\int_\Omega Q_k\left[\mathbf{s}_{u_\alpha}\right]_i dV-\oint_{\Gamma_\Omega}Q_k n_i p_{\mathrm{bc}}d\Gamma,$$

in which k and l are the degrees of freedom of element E and i and j are dimensions. $\boldsymbol{n}^{(E,l)}$ is the normal to the boundary of element E.

Assuming the incompressible flow, the saturation equation can be written as

$$\phi\frac{\partial S_\alpha}{\partial t}+\nabla\cdot\left(\mathbf{u}_\alpha S_\alpha\right)=s_{cty,\alpha}, \tag{6}$$

where ϕ is the porosity and s_{cty} is a source term. This equation is discretised as described in Gomes et al [35] using CVs for the space discretisation and the implicit $\theta-$ method for the time discretisation. Equation 6 is discretised and summed over all the phases, obtaining

$$\sum_{\alpha=1}^{\mathcal{N}_\alpha}\left\{\int_\Omega P_i\frac{\phi\left(S_{\alpha i}^{n+1}-S_{\alpha i}^n\right)}{\Delta t}dV+\oint_{\Gamma_{CV_i}}\left[\theta^{n+\frac{1}{2}}\mathbf{n}\cdot\mathbf{u}_\alpha^{n+1}S_\alpha^{n+1}+\left(1-\theta^{n+\frac{1}{2}}\right)\mathbf{n}\cdot\mathbf{u}_\alpha^n S_\alpha^n\right]\,d\Gamma-\int_\Omega P_i s_{cty,\alpha}^{n+\theta}\,dV\right\}=0. \tag{7}$$

Equation 7 is also bounded by the constraint:

$$\sum_{\alpha=1}^{\mathcal{N}_\alpha}S_{\alpha i}^n=1,\quad \forall n, \tag{8}$$

Solving for $\mathbf{u}^{n+1}$ in matrix form, Equation 7 becomes

$$\mathbf{B}^T\underline{\mathbf{v}}^{n+1}=\underline{\mathbf{s}}_p. \tag{9}$$

The pressure matrix is obtained by manipulating the matrix systems formed by Equations 5 and 9. First, Equation 5 is multiplied by $\mathbf{M}^{-1}$ to yield

$$\underline{\mathbf{v}}=-\mathbf{M}^{-1}\mathbf{C}\underline{\mathbf{p}}+\mathbf{M}^{-1}\underline{\mathbf{s}}_u. \tag{10}$$

The mass matrix ($\mathbf{M}$) is block diagonal. Therefore, its inverse is not very expensive to calculate. Moreover, if a lumped mass matrix is used, the calculation of the inverse is straightforward as the matrix becomes diagonal. Next, Equation 10 is multiplied by $\mathbf{B}^T$:

$$\mathbf{B}^T\underline{\mathbf{v}} = -\mathbf{B}^T\mathbf{M}^{-1}\mathbf{C}\underline{\mathbf{p}} + \mathbf{B}^T\mathbf{M}^{-1}\underline{\mathbf{s}}_u. \tag{11}$$

Combining Equation 11 with Equation 9, to remove the dependency from the velocity, the pressure system is obtained:

$$\mathbf{B}^T\mathbf{M}^{-1}\mathbf{C}\underline{\mathbf{p}}^{n+1} = \underline{\mathbf{s}}_p^{n+1} - \mathbf{B}^T\mathbf{M}^{-1}\underline{\mathbf{s}}_u^{n+1}. \tag{12}$$

The pressure matrix is, therefore, formed by $\mathbf{B}^T\mathbf{M}^{-1}\mathbf{C}$. This pressure matrix needs to be solved using a linear solver. Here, the package PETSc is used as the solver tool.[36] More specifically, to solve the pressure matrix, a GMRES solver with 30 restart iterations and a multigrid preconditioner[37] is used. The preconditioner is either hypre[38] or GAMG[39] both with their default PETSc configurations.

3 | NUMERICAL EXPERIMENTS

The presented formulation is first tested against the semianalytical Buckley-Leverett solution (Model 1). In Model 2, the efficiency to solve the pressure matrix of the DCVFEM is tested against the classical CVFEM in a 3D homogeneous domain with single phase flow. Next, the efficiency to solve the pressure matrix is tested using two 3D test cases with very distorted meshes (see Table 1), one with isotropic (Model 3) and one with anisotropic permeability (Model 4). Models 1, 3, and 4 simulate 2-phase flow and the Brooks-Corey model for relative permeability[40] is used:

$$k_{rw}(S_w) = k_{w_{max}}\left(\frac{S_w - S_{wirr}}{1 - S_{wirr} - S_{nwr}}\right)^{n_w}, \tag{13}$$

$$k_{ro}(S_w) = k_{o_{max}}\left(\frac{S_{nw} - S_{nwr}}{1 - S_{wirr} - S_{nwr}}\right)^{n_{nw}}, \tag{14}$$

where S_w and S_{nw} are the wetting and nonwetting phase saturations, respectively. The irreducible wetting phase saturation (S_{wirr}), Brooks-Corey exponents (n_w and n_{nw}), viscosity ratio (M^0) defined with the viscosity of the wetting phase in the numerator, end-point relative permeability ($k_{w_{max}}$ and $k_{o_{max}}$) and residual nonwetting phase saturation (S_{nwr}) are defined in Table 2. Units are SI except for permeability that is reported in miliDarcy ($1mD = 9.869233 \times 10^{-16}m^2$).

For all multiphase test cases, the domain is initially saturated with the nonwetting phase at $(1 - S_{wirr})$. The wetting phase is injected through the inlet boundary, displacing the nonwetting phase towards the outlet boundary. All other boundaries have no

TABLE 1 Percentage of elements with angles greater than the value shown for the test cases Models 2, 3, and 4

Angle	% Model 2	% Model 3	% Model 4
120	33.33	73.15	54.10
150	33.33	16.03	21.53
170	33.33	1.38	3.88
175	33.33	0.26	0.11

TABLE 2 Fluid properties and boundary conditions for test cases Models 1 to 4

Model	$k_{w_{max}}$	$k_{o_{max}}$	S_{wirr}	S_{nwr}	$n_w = n_{nw}$	M^0	u_{in}	Δp
1	1.0	1.0	0.2	0.3	2.0	10	0.2	N/A
2	N/A	N/A	N/A	N/A	N/A	N/A	0.2	N/A
3	0.3	0.8	0.2	0.2	2.0	4	N/A	5.48×10^7
4	1.0	1.0	0.2	0.2	2.0	10	2.6×10^{-7}	N/A

Abbreviation: N/A, not applicable.

flow. For Models 1, 2, and 4, the wetting phase is injected at a constant rate u_{in}; for Model 3 injection is at constant pressure yielding a fixed pressure drop Δp. Porosity and horizontal (K_h) and vertical (K_v) permeabilities are specified in Table 3 for the different test cases and domains R1 to R3 of the heterogeneous test cases.

3.1 | Model 1: 1D immiscible displacement

In the first numerical experiment, the DCVFEM is tested against the 1D Buckley-Leverett (BL) solution,[41] in which a nonwetting phase is displaced by a wetting phase. First, the element pair $P_0DGP_1(CV)$ is tested. The saturation profile using different meshes is shown in Figure 2, and error metrics are shown in Figure 3. Likewise, the element pair $P_1DGP_2(CV)$ is tested. Figure 4 shows the saturation profile using different meshes. Both element pairs are able to capture the shock front (sharp saturation change), the rarefaction (smooth saturation change behind the shock front), and conserve mass. Figure 3 shows the corresponding errors compared with the classical CVFEM. Figure 3A shows that for a given resolution and using the element pair P_0DGP_1, the classical formulation CVFEM yields a more accurate result, although the difference in accuracy between the methods is small for a given mesh resolution. Figure 3B, on the other hand, shows that for a given resolution and using the element pair P_1DGP_2,

TABLE 3 Geological properties for test cases Models 1 to 4

Model	R_1			R_2			R_3		
	ϕ	K_h	K_v	ϕ	K_h	K_v	ϕ	K_h	K_v
1	0.2	1.0	1.0	N/A	N/A	N/A	N/A	N/A	N/A
2	0.2	1.0	1.0	N/A	N/A	N/A	N/A	N/A	N/A
3	0.2	1000	1000	0.2	200	200	0.2	50	50
4	0.27	200	200	0.24	20	2	0.2	2	0.02

Abbreviation: N/A, not applicable.

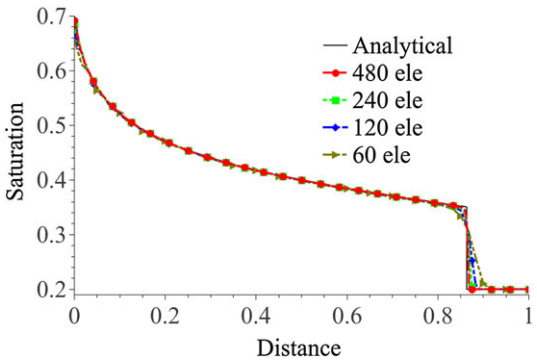

FIGURE 2 Snapshot in time showing wetting phase saturation as a function of dimensionless distance, comparing the analytic BL solution to the numerical solutions using the $P_0DGP_1(CV)$ element pair for various 2D simulations with 4 elements in the Y direction and 60, 120, 240, and 480 elements in the X direction [Colour figure can be viewed at wileyonlinelibrary.com]

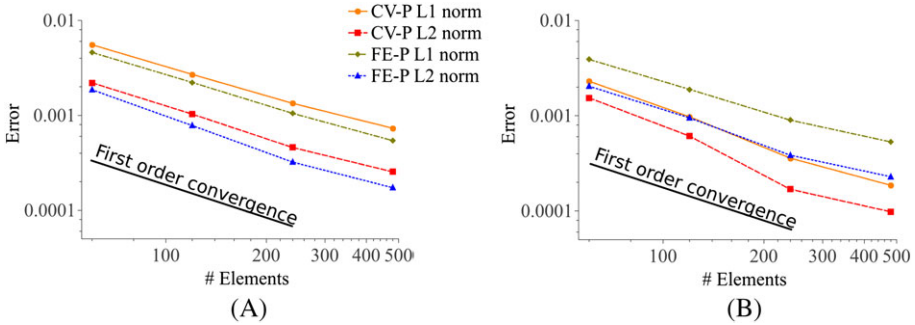

FIGURE 3 L_1- and L_2-error norms using the classical control volume finite element method and the new double control volume finite element method for various 2D simulations with 4 elements in the Y direction and 60, 120, 240, and 480 elements in the X direction. A, Errors using the element pair $P_0DGP_1(CV)$ and $P_0DGP_1(FE)$. B, Errors using the element pair $P_1DGP_2(CV)$ and $P_1DGP_2(FE)$. CV, control volume; FE, finite element [Colour figure can be viewed at wileyonlinelibrary.com]

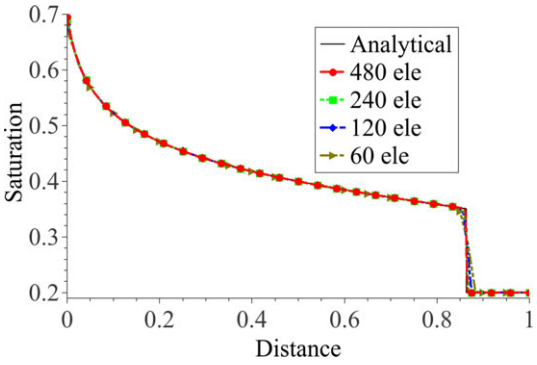

FIGURE 4 Snapshot in time showing wetting phase saturation as a function of dimensionless distance, comparing the analytic BL solution to the numerical solutions using the $P_1DGP_2(CV)$ element pair for various 2D simulations with 4 elements in the Y direction and 60, 120, 240, and 480 elements in the X direction [Colour figure can be viewed at wileyonlinelibrary.com]

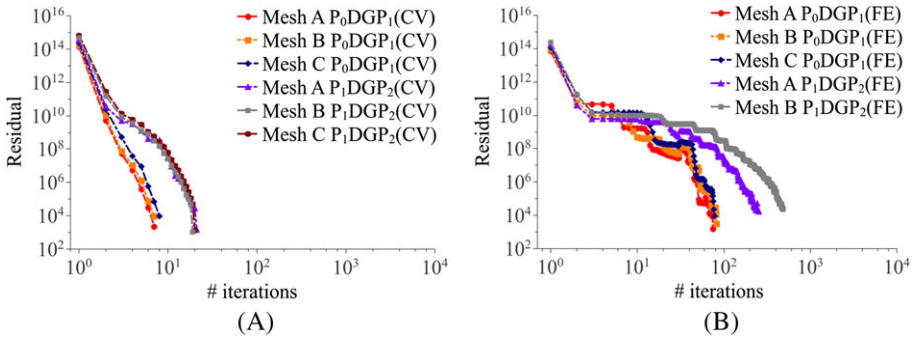

FIGURE 5 Residual reduction versus the number of iterations for the initial time-step using GMRES(30) + hypre as solver for the A, double control volume finite element method method and the B, classical control volume finite element method (CVFEM). The classical CVFEM showed no convergence for Mesh C and the P1DGP2(FE) element pair so these results are not shown. CV, control volume; FE, finite element [Colour figure can be viewed at wileyonlinelibrary.com]

the new DCVFEM formulation yields a more accurate result although the difference is again small. Note that flux limiters (see Gomes et al [35]) revert to a low accuracy (first-order method) advection scheme around the shock front, so in this example problem, the DCVFEM yields slightly higher accuracy than the classical CVFEM for quadratic elements. The most significant finding here is that the new DCVFEM method has a similar quality of match to a known solution as the conventional CVFEM.

These experiments show that the new DCVFEM formulation can correctly model multiphase flow. As in Gomes et al, [35] the results show close-to-linear convergence (Figure 3), which is the best that can be expected due to the requirement of flux-limiting to correctly capture the shock-front. [42] This result is important because the close-to-linear convergence obtained in Gomes et al [35] is very uncommon in the literature. Usually the observed convergence is 0.5 (see, for example, Schmid et al, [10] Abushaikha et al, [12] and Hoteit and Firoozabadi [43]). Discretising the pressure using CVs does not affect the order of convergence of the method.

3.2 | Model 2: 3D homogeneous case

In this case, the new DCVFEM is tested against the classical CVFEM in a test case in which both numerical methods can solve the pressure system using the iterative solver GMRES with 30 restart iterations with hypre as preconditioner. The domain has homogeneous material properties and only one fluid phase is considered. The aspect ratio of the problem is very high (1:1000), and the mesh has been distorted intentionally to obtain a poor quality mesh with a 33.33% of the elements with angles above 175° (Table 1).

Three different meshes are tested to evaluate the efficiency of the proposed method. Mesh A is defined by 3000 elements. Meshes B and C are created by refining-by-splitting mesh A. Mesh B is defined by 24 000 elements and mesh C by 192 000 elements.

Figure 5 shows the residual reduction versus the number of iterations for the different meshes and element pairs using the classical CVFEM and the novel DCVFEM. The DCVFEM can always achieve convergence and the number of iterations to

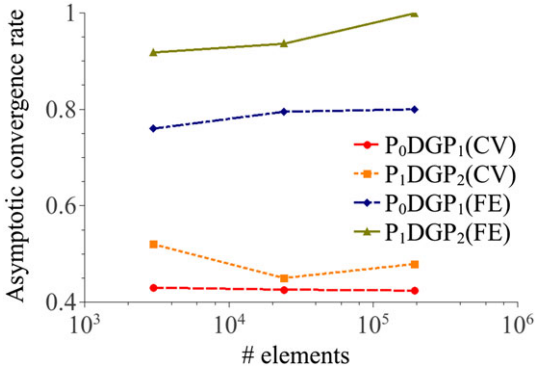

FIGURE 6 Asymptotic convergence rates for the different combination of meshes/formulations. The double control volume finite element method shows consistently a better asymptotic convergence rate than the classical control volume finite element method. CV, control volume; FE, finite element [Colour figure can be viewed at wileyonlinelibrary.com]

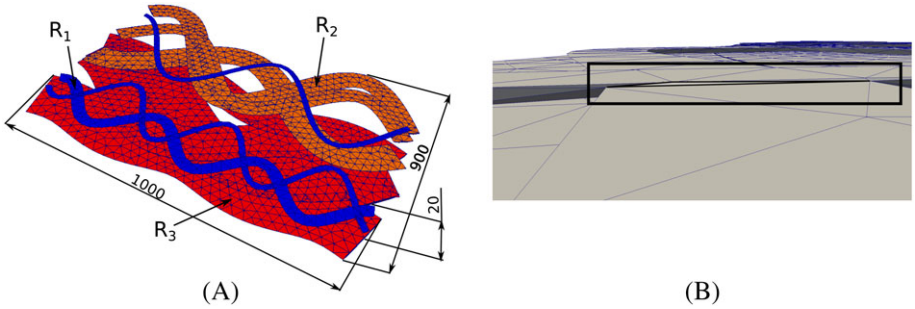

FIGURE 7 A, Numerical model with the corresponding mesh (12 854 elements) and 3 different domain types with different material properties (labelled R1-R3; corresponding material properties shown in Table 3). B, Close-up showing the subdomain created by the intersection of 2 channels; an element, highlighted, with a very obtuse angle (>175°), is created as a consequence of this intersection. Many other similar intersections are present in the model [Colour figure can be viewed at wileyonlinelibrary.com]

reduce the residual; 10 orders of magnitude is much smaller than when using the classical CVFEM, requiring 1 or 2 orders of magnitude fewer iterations. Moreover, Figure 6 displays the asymptotic convergence rates for both methods. The DCVFEM shows a significantly better asymptotic convergence rate than the classical CVFEM.

3.3 | Model 3: 3D test case representing a common subsurface geological reservoir containing channelized sandbodies

This numerical experiment uses a heterogeneous 3D model that captures channelized features typical of many subsurface geological reservoirs, including hydrocarbon reservoirs, aquifers, and targets for geological CO_2 storage. The model contains 3 types of channelized sandbody, each with a different value of (isotropic) permeability, in a zero permeability mudstone background (not shown) (see Figure 7A and Jacquemyn et al [44]). The aspect ratio of the problem is very large (Figure 7A). Moreover, the subdomains created because of the intersections between different channels have even higher aspect ratios (Figure 7B). Consequently, high aspect ratio ("sliver") elements with large angles are introduced in the mesh unless a very large number of small elements are used. Moreover, there are large contrasts in permeability between domains (Table 3). Such features are typical of subsurface reservoirs it is important that models can capture their geometries and correctly simulate multiphase flow.

Three different meshes are tested to evaluate the efficiency of the proposed method. Mesh A is defined by 12 854 elements (Figure 7). Meshes B and C are created by refining-by-splitting mesh A. Mesh B is defined by 102 832 elements and mesh C by 824 464 elements. The mesh quality in this numerical experiment is characterized by the angles defined in Table 1. It can be seen that the elements are very distorted, with the majority having an angle >120° and a significant number >170°.

Figure 8 shows the residual reduction versus the number of iterations for the different meshes and element pairs using GMRES with 30 restart iterations together with hypre (Figure 8A) or GAMG (Figure 8B) preconditioners. It can be seen that the number of iterations is very low in all cases, especially using hypre as the preconditioner. Moreover, Figure 9 shows the asymptotic convergence rate for the different methods/resolutions. Using hypre, the convergence rate is almost independent of the mesh

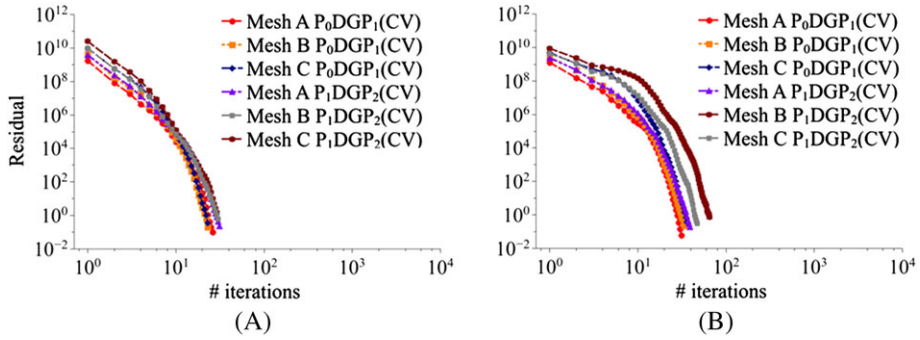

FIGURE 8 Residual reduction versus the number of iterations for the initial time-step for the double control volume finite element method. No control volume finite element method results are shown as none of the solvers were able to achieve convergence. A, The results using GMRES(30) + hypre. B, The results using GMRES(30) + GAMG. CV, control volume [Colour figure can be viewed at wileyonlinelibrary.com]

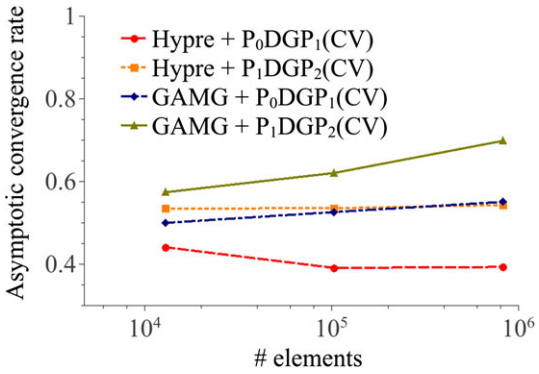

FIGURE 9 Asymptotic convergence rates for the different combinations of meshes/solvers. The hypre preconditioner performs better as it shows a mesh independent convergence rate. CV, control volume [Colour figure can be viewed at wileyonlinelibrary.com]

used and there is only a small variation using GAMG. The convergence rate is especially good for the $P_0DGP_1(CV)$ element pair. However, even the high-order element pair $P_1DGP_2(CV)$ shows mesh independent performance.

It is important to note that using the classical CVFEM approach, no convergence could be achieved using this set of iterative solvers. With the new method presented here, the asymptotic convergence rates obtained are very good considering the quality of the mesh and the significant permeability contrasts between domains.

3.4 | Model 4: 3D test case representing a common subsurface geological reservoir deposited in a shallow marine environment

We finish testing the new method by using a second heterogeneous 3D model of complex but common geological features to demonstrate that the method is robust. In this case, the model contains 3 different domains with different material properties, representing different types of sandstone deposited in a shallow marine environment.[26,27,32] The geometry of the domains is partially controlled by curved, inclined surfaces termed clinoforms. These clinoform surfaces intersect and create wedge-shaped, high aspect-ratio features. Meshing algorithms typically create large-angle elements around these features. The contrasts in material properties across domains are again very large (see Table 3). Moreover, in this example, the permeability in the different domains is anisotropic. Figure 10 shows the numerical domain with the corresponding dimensions, regions and mesh (36 160 elements).

Three different meshes are tested to evaluate the efficiency of the proposed method. Mesh A is defined by 36 160 elements (Figure 10). Meshes B and C are created by refining-by-splitting mesh A. Mesh B is defined by 289 280 elements and mesh C by 2 314 240 elements. The mesh quality is again characterized by the angles defined in Table 1. Similar to the previous test case, the elements are very distorted. In this case, there are more elements with angles >150° and also more elements with angles >170°, making this numerical experiment more challenging.

Figure 11 shows the residual reduction versus the number of iterations for the different meshes and element pairs using GMRES with 30 restart iterations together with hypre (Figure 11A) and GAMG (Figure 11B). In all cases, the number of

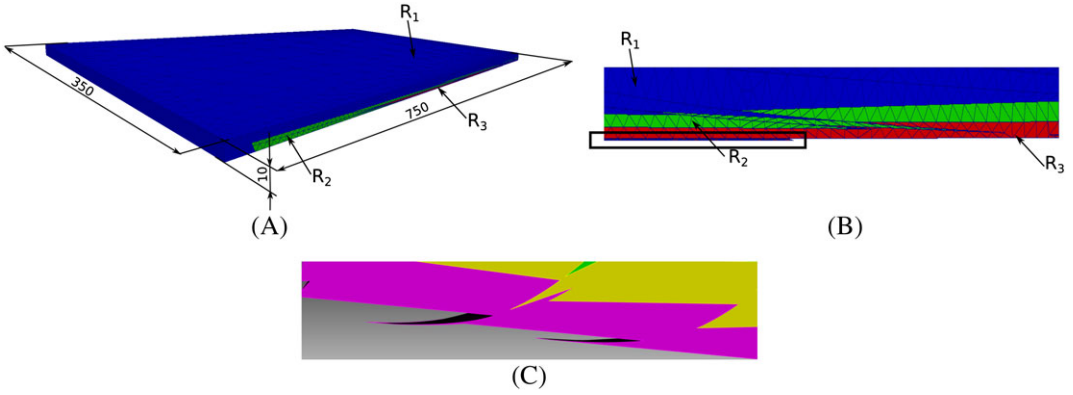

FIGURE 10 A, Numerical domain with the corresponding mesh (36 160 elements), domain sizes, and the 3 regions with different geological properties. B, Two-dimensional section (vertically exaggerated by two) seen from 1 side, with the 3 regions defined. The rectangle surrounds one of the extremely high aspect ratio features of this numerical experiment. C, View 20× exaggerated in the vertical direction, displaying some of the highest aspect ratio features of the domain, corresponding to the rectangle shown in panel B. The elements used in these regions are defined by angles over 175°; some even have angles above 179° [Colour figure can be viewed at wileyonlinelibrary.com]

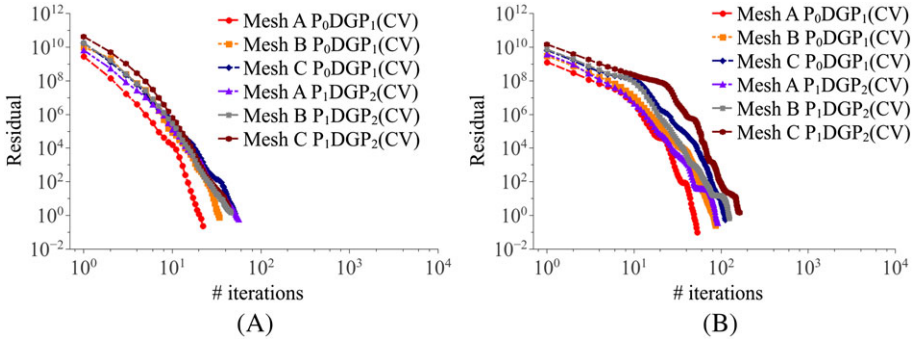

FIGURE 11 Residual reduction versus the number of iterations for the initial time-step for the double control volume finite element method. No control volume finite element method results are shown as none of the solvers were able to achieve convergence. A, Results using hypre. B, Results using GAMG. CV, control volume [Colour figure can be viewed at wileyonlinelibrary.com]

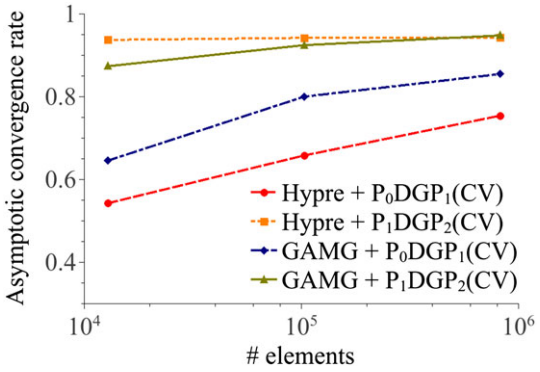

FIGURE 12 Asymptotic convergence rates for the different combination of meshes/solvers. Due to the complexity of this problem there is no mesh independent convergence rate. CV, control volume [Colour figure can be viewed at wileyonlinelibrary.com]

iterations is below 200. Moreover, when using hypre as a preconditioner, the number of iterations is always below 60. However, contrary to the previous numerical experiment, the convergence here does depend on the mesh. Nonetheless, considering the difficulty of the numerical experiment, the results obtained are very satisfactory, as the number of iterations is very low even when the mesh has more than 2 million elements. Figure 12 shows the asymptotic convergence rate for the different

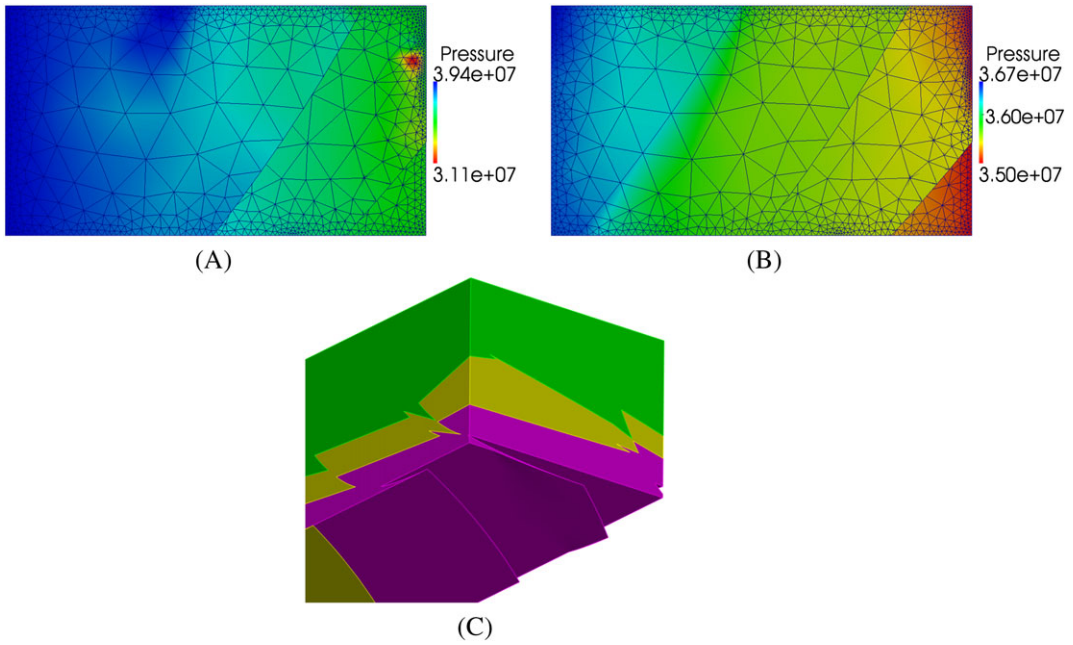

FIGURE 13 A, View from below of the pressure field using the classical control volume finite element method approach. A nonphysical pressure drop can be seen close to the right boundary. B, View from below of the pressure field obtained using the double control volume finite element method approach. C, 20× vertically exaggerated view of the model from below displaying the high aspect ratio wedge-shaped domains defined by the intersecting clinoforms [Colour figure can be viewed at wileyonlinelibrary.com]

methods/resolutions. The asymptotic convergence is not as good as in Model 2 and, in some cases, is above 0.9. However, as seen in Figure 11, the convergence rate to reduce the residual by 10 orders of magnitude, which is usually sufficient to obtain the correct numerical solution, is reasonable. Moreover, it is important to note that using the classical CVFEM approach, no convergence could be achieved using this set of iterative solvers.

As an example of the robustness of the new DCVFEM approach, the CVFEM was used with mesh A and the low-order element pair $P_0DGP_1(CV)$ to obtain the pressure field using a direct solver. Figure 13A shows that the result is clearly nonphysical and therefore incorrect (notice the nonphysical pressure drop near the right boundary). Using the new DCVFEM, the pressure field is as expected (Figure 13B). Figure 13C shows the connectivity between the different layers of the numerical domain. The new DCVFEM presented here is able to properly calculate the pressure field using an iterative solver with no special modifications. Classical CVFEM formulations do not converge using an iterative solver and yield incorrect solutions using a direct solver.

4 | CONCLUSIONS

A novel, high-order, DCVFEM with $n-1$th-order representation for velocity and nth-order for pressure is presented. The new formulation is based on the well-known CVFEM and retains desirable features such as mass conservation. Its implementation in a conventional CVFEM code requires the use of CV shape functions to discretise the pressure. The novelty of the formulation is that it provides significantly better pressure matrices in complex heterogeneous problems. This is important because many problems of interest, particularly those focused on subsurface geological reservoirs, contain complex geometries with very high aspect ratio domains. These produce mesh elements with large angles unless very high resolution is used which is computationally expensive. The new method enables solutions to be obtained using iterative numerical solvers for meshes where classical CVFEM fails. It also allows convergence to be achieved in fewer iterations in models where both methods work.

The new formulation yields accurate solutions with first-order convergence when tested against the classical Buckley-Leverett benchmark. Simulations of heterogeneous test cases demonstrate that new method shows better performance than classical CVFEM, as it is always able to solve the pressure system using a black box iterative solver and good convergence rates are achieved even in models with highly distorted meshes. Moreover, the new method correctly calculates the pressure field in cases where the classical CVFEM fails even using a direct solver.

ACKNOWLEDGEMENTS

Funding for Salinas from ExxonMobil is gratefully acknowledged. Pavlidis would like to acknowledge the support from: EPSRC "Reactor Core-Structure Relocation Modelling for Severe Nuclear Accident" and Horizon 2020 "In-Vessel Melt Retention". Xie is supported by EPSRC ("Multi-Scale Exploration of Multiphase Physics in Flows"—MEMPHIS). Part funding for Jackson under the TOTAL Chairs programme at Imperial College is also acknowledged. No data was generated in the course of this work. For further information, please contact the corresponding author at (pablo.salinas@imperial.ac.uk) the AMCG Group (www.imperial.ac.uk/earth-science/research/research-groups/amcg/) or the NORMS group (www.imperial.ac.uk/earth-science/research/research-groups/norms) as required.

REFERENCES

1. Aziz K, Settari A. *Petroleum Reservoir Simulation*. London: Applied Science Publishers; 1979.
2. Chen Z, Ewing R. Comparison of various formulations of three-phase flow in porous media. *J Comput Phys*. 1997;132(2):362–373.
3. Forsyth P. A control volume finite element approach to NAPL groundwater contamination. *SIAM J Sci Stat Comput*. 1991;12:1029–1057.
4. Fung L, Hiebert A, Nghiem L. Reservoir simulation with control-volume finite element method. *SPE Reservoir Eng*. 1992;7(3):349–357.
5. Durlofsky L. A triangle based mixed finite element finite volume technique for modelling two-phase flow through porous media. *J Comput Phys*. 1993;105:252–266.
6. Durlofsky L. Accuracy of mixed and control volume finite element approximations to Darcy velocity and related quantities. *Water Resour Res*. 1994;30:965–973.
7. Geiger S, Roberts S, Matthäi S, Zoppou C, Burri AA. Combining finite element and finite volume methods for efficient multiphase flow simulations in highly heterogeneous and structurally complex geologic media. *Geofluids*. 2004;4(4):284–299.
8. Wheeler M, Yotov I. A multipoint flux mixed finite element method. *SIAM J Numer Anal*. 2006;44:2082–2106.
9. Matthai S, Mezentsev A, Belayneh M. Finite element-node centered finite-volume two-phase flow experiments with fractured rock represented by unstructured hybrid element meshes. *SPE*. 2007;93341:740–756.
10. Schmid K, Geiger S, Sorbie K. Higher order FE–FV method on unstructured grids for transport and two-phase flow with variable viscosity in heterogeneous porous media. *J Comput Phys*. 2013;241(0):416–444.
11. Jackson MD, Percival J, Mostaghimi P, Tollit BS., D. Pavlidis CP, Gomes JLMA., El-Sheikh AH., Salinas AMP, Blunt M. Reservoir modeling for flow simulation by use of surfaces, adaptive unstructured meshes, and an overlapping-control-volume finite-element method. *SPE Reservoir Eval Eng*. 2015;18:115–132.
12. Abushaikha A, Blunt M, Gosselin O, Pain C, Jackson MD. Interface control volume finite element method for modelling multi-phase fluid flow in highly heterogeneous and fractured reservoirs. *J Comput Phys*. 2015:41–61.
13. Mostaghimi P, Percival J, Pavlidis D, Ferrier R, Gomes J, Gorman G, Jackson MD, Neethling S, Pain C. Anisotropic mesh adaptivity and control volume finite element methods for nucmerical simulation of multiphase flow in porous media. *Math Geosci*. 2015;347:673–676.
14. Salinas P, Percival JR, Pavlidis D, Xie Z, Gomes J, Pain CC, Jackson MD. A discontinuous overlapping control volume finite element method for multi-phase porous media flow using dynamic unstructured mesh optimization. Spe 173279; 2015; SPE Reservoir Simulation Symposium, Houston, Texas, USA. 1–18.
15. Aziz I, Babuska AK. On the angle condition in the finite-element method. *SIAM J Numer Anal*. 1976;13:214–226.
16. Shewchuk J. What is a good linear finite element? Interpolation, conditioning, anisotropy, and quality measures. 11th International Meshing Roundtable; 2002; Ithaca, New York. 1–65.
17. Venditti D. An H-Adaptive Control-Volume Finite Element Method for Steady, Two-Dimensional Fluid Flow and Heat Transfer. *Ph.D. Thesis*; 1998.
18. Larreteguy AE. An equal-order control-volume finite-element method for fluid flow in arbritrary triangulations. *Numer Heat Transfer, Part B: Fundam*. 1995;28:4:401–413.
19. Shewchuck JR. Triangle: engineering a 2D quality mesh generator and Delaunay triangulator. *Appl Comput Geom Towards Geom Eng*. 1996;22:21–74.
20. Shewchuk J. Delaunay refinement algorithms for triangular mesh generation. *Comput Geom*. 2002;22(1):21–74.
21. Erten AUH. Quality triangulations with locally optimal steiner points. *SIAM J Sci Comput*. 2009;31:2103–2130.
22. Erten AUH. Computing triangulations without small and large angles. *Int Symp Voronoi Diagrams (ISVD)*. 2009;31:2103–2130.
23. Si H. TetGen, a Delaunay-based quality tetrahedral mesh generator. *ACM Trans Math Softw*. 2015;41(2):11:1–11:36.
24. Alauzet F, Loseille A. A decade of progress on anisotropic mesh adaptation for computational fluid dynamics. *Comput-Aided Des*. 2016;72:13–39. 23rd International Meshing Roundtable Special Issue: Advances in Mesh Generation.
25. Massart B, Jackson MD, Hampson G, Johnson H, Legler B, Jackson CL. Effective flow properties of heterolithic, cross-bedded tidal sandstones: part 1. *AAPG Bull*. 2016;100:697–721.
26. Graham G, Jackson MD, Hampson G. Three-dimensional modeling of clinoforms in shallow-marine reservoirs: part 1. Concepts and application. *AAPG Bull*. 2015;99:1013–1047.
27. Deveugle P, Jackson MD, Hampson G, Farrell M, Sprague A, Stewart J, Calvert C. Characterization of stratigraphic architecture and its impact on fluid flow in a fluvial-dominated deltaic reservoir analog: upper Cretaceous Ferron sandstone member, Utah. *AAPG Bull*. 2011;95:693–727.
28. Jackson MD, Yoshida S, Muggeridge AH, Johnson HD. Three-dimensional reservoir characterization and flow simulation of heterolithic tidal sandstones. *AAPG Bull*. 2005;89(4):507–528.

29. Pavlidis D, Gomes JLMA, Xie Z, Percival JR, Pain CC, Matar OK. Compressive advection and multi-component methods for interface-capturing. *Int J Numer Methods Fluids*. 2016;80(4):256–282.
30. Salinas P, Pavlidis D, Xie Z, Adam A, Pain CC, Jackson MD. Improving the convergence behaviour of a fixed-point-iteration solver for multiphase flow in porous media. *Int J Numer Methods Fluids*. 2016. https://doi.org/10.1002/fld.4357. Accessed December 2016.
31. Xie Z, Pavlidis D, Salinas P, Percival J, Pain C, Matar O. A balanced-force control volume finite element method for interfacial flows with surface tension using adaptive anisotropic unstructured meshes. *Comput Fluids*. 2016;138:38–50.
32. Sech R, Jackson MD, Hampson G. Three-dimensional modeling of a shoreface-shelf parasequence reservoir analog: part 1. Surface-based modeling to capture high-resolution facies architecture. *AAPG Bulletin*. 2009;93(9):1155–1181. https://doi.org/10.1306/05110908144
33. Jackson MD, Gomes J, Mostaghimi P, Percival J, Tollit B, Pavlidis CPD, El-Sheikh AMAH, Blunt M. Reservoir modeling for flow simulation using surfaces, adaptive unstructured meshes and control-volume-finite-element methods. Spe 163633; 2013; Houston, Texas.
34. Melnikova Y, Jacquemyn C, Osman H, Salinas P, Gorman G, Hampson G, Jackson MD. Reservoir modelling using parametric surfaces and dynamically adaptive fully unstructured grids. In: ECMOR XV - 15th European Conference on the Mathematics of Oil Recovery; 2016; Amsterdam, The Netherlands. 1–9.
35. Gomes J, Pavlidis D, Salinas P, Xie Z, Percival J, Melnikova Y, Pain C, Jackson MD. A force-balanced control volume finite element method for multiphase porous media flow modelling. *Int J Numer Meth Fluids*. 2016. https://doi.org/10.1002/fld.4275. Accessed August 2016
36. Balay S, Gropp W, McInnes L, Smith B. Efficient management of parallelism in object-oriented numerical software libraries. 1997:163–202.
37. Brandt A. Multilevel adaptive solutions to boundary-value problems. *Math Comput*. 1977;31:333–390.
38. Falgout RD, Yang UM, Jones JE. Pursuing scalability for hypre's conceptual interfaces. *ACM Trans. Math. Software*. 2005;31(3):326–350.
39. Adams M. Algebraic multigrid methods for constrained linear systems with applications to contact problems in solid mechanics. 2007;39:141–153.
40. Brooks R, Corey A. *Hydrology Papers*, Vol. 3. Fort Collins: Colorado State University; 1964.
41. Buckley S, Leverett M. Mechanism of fluid displacements in sands. *Trans AIME*. 1942;146:107–116.
42. Harten A, Hyman J, Lax P. On finite-difference approximations and entropy conditions for shocks. *Commun Pure Appl Math*. 1976; 29(3):297–322.
43. Hoteit H, Firoozabadi A. Numerical modeling of two-phase flow in heterogeneous permeable media with different capillarity pressures. *Adv Water Res*. 2008;31(1):56–73.
44. Jacquemyn C, Melnikova Y, Jackson MD, Hampson G, John C. Geologic modelling using parametric nurbs surfaces. In: ECMOR XV - 15th European Conference on the Mathematics of Oil Recovery. Amsterdam, The Netherlands, 2016; 1–10.

How to cite this article: Salinas P, Pavlidis D, Xie Z, et al. Improving the Robustness of the Control Volume Finite Element Method with Application to Multiphase Porous Media Flow. *Int J Numer Meth Fluids*. 2017;0:1–12. https://doi.org/10.1002/fld.4381